Ultra-Thin Hollow Carbon Nanospheres for Pseudocapacitive Sodium-Ion Storage

Young Soo Yun,[a] Se Youn Cho,[b] Haegyeom Kim,[a] Hyoung-Joon Jin,*[b] and Kisuk Kang*[a, c]

Ultra-thin hollow carbon nanospheres (UTH-CNs) are fabricated for use as anodes of asymmetric sodium ion pseudocapacitors. The ~3 nm thick amorphous carbon walls obtained from re-generated silk proteins as a template exhibit a well-defined porous structure suitable for reversible sodium-ion storage. The UTH-CNs show remarkable electrochemical activity with sodium via a pseudocapacitive reaction, delivering a large re-versible capacity as well as superior rate performance for more than 1000 cycles. The pseudocapacitors based on UTH-CNs exhibit a capacitance of 186 F g^{-1}, a specific energy of 43 Wh kg^{-1} and a power density of 10 kW kg^{-1}. This represents the highest value yet reported for asymmetric sodium-ion storage pseudo-capacitors.

1. Introduction

Electrical energy storage has become increasingly important in recent years. The rapid increase in demand for mobile electronics and emerging electric transportation applications requires cost-effective energy storage systems with improved energy and power capacities.[1–3] Conventional lithium-ion batteries (LIBs) are important for smaller electronics devices because of the high energy density (typically 150–200 Wh kg^{-1}). However, emerging applications, particularly electric vehicles, require exceptionally long cycle stability ($>$ 10 years) and a high power density ($>$ 1,000 W kg^{-1}) with a substantially lower cost than currently available technology.[4] Electrochemical capacitors (also known as supercapacitors) exhibit a high power density of ~10 kW kg^{-1} with reliable cycle stability, but they are limited by a low energy density of 5–10 Wh kg^{-1}.[4,5] Given these limitations, as well as the potential applications, much effort has been made to bridge the performance gap between the LIBs and electrochemical capacitors, with the aim of achieving both a high energy density and a high power density.[5–10]

One approach to addressing this issue is to combine the electrode configurations of both devices using a faradaic electrode on one side, with a non-faradaic capacitive electrode on the other side.[11–14] This configuration stores charge asymmetrically via faradaic and non-faradaic capacitive reactions, respectively. The fast surface adsorption/desorption at the capacitive electrode results in a favorable overall power capability of the device, and a high energy density can be achieved using the faradaic electrode. The principal issue with combining these two different electrodes in such asymmetric supercapacitors is an imbalance in the power capability, because faradaic reactions are much slower than non-faradaic capacitive charge storage. This kinetic imbalance limits the overall performance, so proper selection of a rapid-response faradaic electrode is particularly important.[11–14]

Various nanostructured carbon materials (NSCMs) have been demonstrated as high-power faradaic electrodes,[15–21] with potential for applications as counter electrodes in asymmetric supercapacitors. These can be expected to exhibit a high power density due to the short transport path for ions and electrons, delivering relatively high capacity via intercalation of ions into the carbon structure. Moreover, pseudocapacitor-like behavior has been observed for some of the NSCM-based faradaic electrodes when storing ions, including lithium and sodium, which further increases the power density.[22] One interesting observation is that sodium ions can be stored as fast as lithium ions in NSCMs, despite the relatively large size of sodium ions. This is likely due to the pseudocapacitive behavior, which is less sensitive to the bulk diffusion of ions.[23–25] It should be noted that in contrast to lithium intercalation, sodium intercalation into graphitic layers is considered impractical because of the small interlayer space.[26] Considering the similarity to lithium-ion storage in terms of chemistry, and the relative abundance of sodium, it follows that asymmetric sodium-ion supercapacitors using pseudocapacitive NSCM as a faradaic electrode have potential as a viable alternative to conventional LIBs for energy storage.

Here, we report ultra-thin hollow carbon nanospheres (UTH-CNs) as a faradaic electrode material for asymmetric sodium-ion supercapacitors. By exploiting the hollow morphology, we aimed to further increase the power by reducing the thickness

[a] Dr. Y. S. Yun, Prof. H. Kim, Prof. K. Kang
Materials Science and Engineering
Research Institute of Advanced Materials (RIAM)
Seoul National University, Seoul 151-742 (South Korea)
E-mail: matlgen1@snu.ac.kr

[b] S. Y. Cho, H.-J. Jin
Polymer Science and Engineering
Inha University, Incheon 402-751 (South Korea)

[c] Prof. K. Kang
Center for Nanoparticles Research, Institute for Basic Science (IBS)
Seoul National University, Seoul 151-742 (South Korea)

of the walls of the UTH-CNs, as well as by doping them with nitrogen. The ~3 nm thick carbon walls can be expected to lead to rapid sodium-ion kinetics, and to provide a large mass density of sodium sites in the NSCM. Furthermore, doping with nitrogen modifies the electronic structure, leading to an increase in the density of electron donor states.[27–29] This modification of the electronic structure may also be expected to increase the electrical conductivity, increase the wettability in an organic electrolyte, and provide more sites for coordinating sodium ions.

2. Results and Discussion

The UTH-CNs were prepared using a naturally occurring polymer (i.e., silk produced by the *Bombyx mori* silk worm) via a template method, followed by carbonization. Silk fibroin is composed of large internal hydrophobic blocks capped with hydrophilic blocks.[30] It can be dissolved and easily reformed into various morphologies resulting from self-assembly.[31–35] This recombined silk fibroin (RSF) can be further transformed into a nanostructured, nitrogen-doped, carbon-based material via a simple pyrolysis process.[5] The fabrication process of the UTH-CNs is shown in Figure 1. The stability of the RSF solution
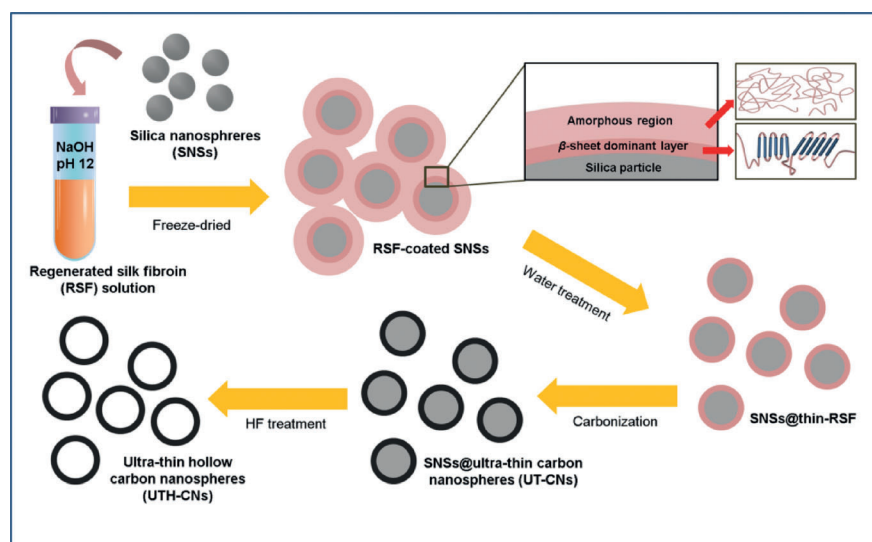
**Figure 1.** Schematic diagram showing the fabrication process for the UTH-CNs.

in the presence of silica nanospheres (SNSs) is pH-dependent.[36] At neutral pH, RSF aggregates to form a gel upon addition of SNSs because of the metastable state of the RSF solution. However, in an alkali solution (pH ≥ 12), RSF solutions are stabilized and become well-dispersed with the SNSs. Following freeze-drying such an alkali mixture, the SNSs become coated with a layer of RSFs. It is known that the surface interaction between RSFs and SNSs leads to the coating of RSFs on the SNSs, rather than phase segregation.[37] No artificial crystallization step was included, which left a relatively large amount of amorphous RSF on the surface of SNS. The amorphous RSF was mainly removed by washing with water. However, a thin

layer of RSF remained on the surface after washing, which was coordinated in a β-sheet crystal structure (see Figure S1). The high pH of the solution is believed to induce negative charges on the SNS surface, prompting formation of the β-sheet structure.[37,38] The thin β-sheet layers were then transformed into carbonaceous materials by heating to 800 °C in an inert gas atmosphere. Following the thermal treatment, the SNSs were removed using HF, yielding the UTH-CNs.

Figures 2 a,b show FE-TEM images of the UTH-CNs, which exhibited a hollow structure composed of thin-walled carbonaceous materials. The wall thickness was approximately 3 nm, as shown in Figure 2 c. The morphology of the UTH-CNs could be distinguished from that of other samples prepared via a similar procedure, but without the washing step. Those samples appeared aggregated, and shared the thick carbonaceous walls with each other (see Figure S2). The XRD data shown in Figure 2 d reveals a broad peak at 24°, corresponding to a lattice spacing of $d = 3.7$ Å, which indicates the degree of stacking order of the layered carbon structure. The weak peak at 43.8° was assigned to the (100) plane, corresponding to the formation of an ordered hexagonal structure. The Raman spectrum shown in Figure 2 e reveals broad D and G band peaks; the D band at ~1342 cm^{-1} corresponds to disorder originating from sp^3-bonded carbon in the UTH-CNs, and the G band at ~1580 cm^{-1} can be assigned to the graphitic structure. The peak intensity ratio of the D to the G was $I_D/I_G = 1.33$. The height L_c and width L_a of the graphitic crystals was calculated from the observed 002 peak in the XRD data, along with the ratio I_D/I_G from the Raman spectrum; L_c was ~1 nm and L_a was ~3.5 nm. These results suggest that the graphitic carbon was a similar size to the basic structural unit (BSU), which is conventionally defined as a planar aromatic structure of fewer than 10–20 hexagonal rings with 2–4 graphitic layers.[39]

The porosity of the UTH-CNs was characterized by nitrogen adsorption and desorption experiments. The nitrogen adsorption and desorption isotherm curves shown in Figure 2 f are indicative of an IUPAC type I microporous structure. The minor H4-type hysteresis in the desorption curve indicates the presence of a small number of mesopores with a narrow slit-like pore structure. The Brunauer–Emmett–Teller (BET)-specific surface area of the UTH-CNs was 400 m^{2}g^{-1}, and the width of most of the micropores was less than a nanometer (see the inset of Figure 2 f). The random distribution of the small graphitic carbon structures and the microporous characteristics are expected to be advantageous for pseudocapacitive sodium-ion storage. However, the resulting electron pathways passing
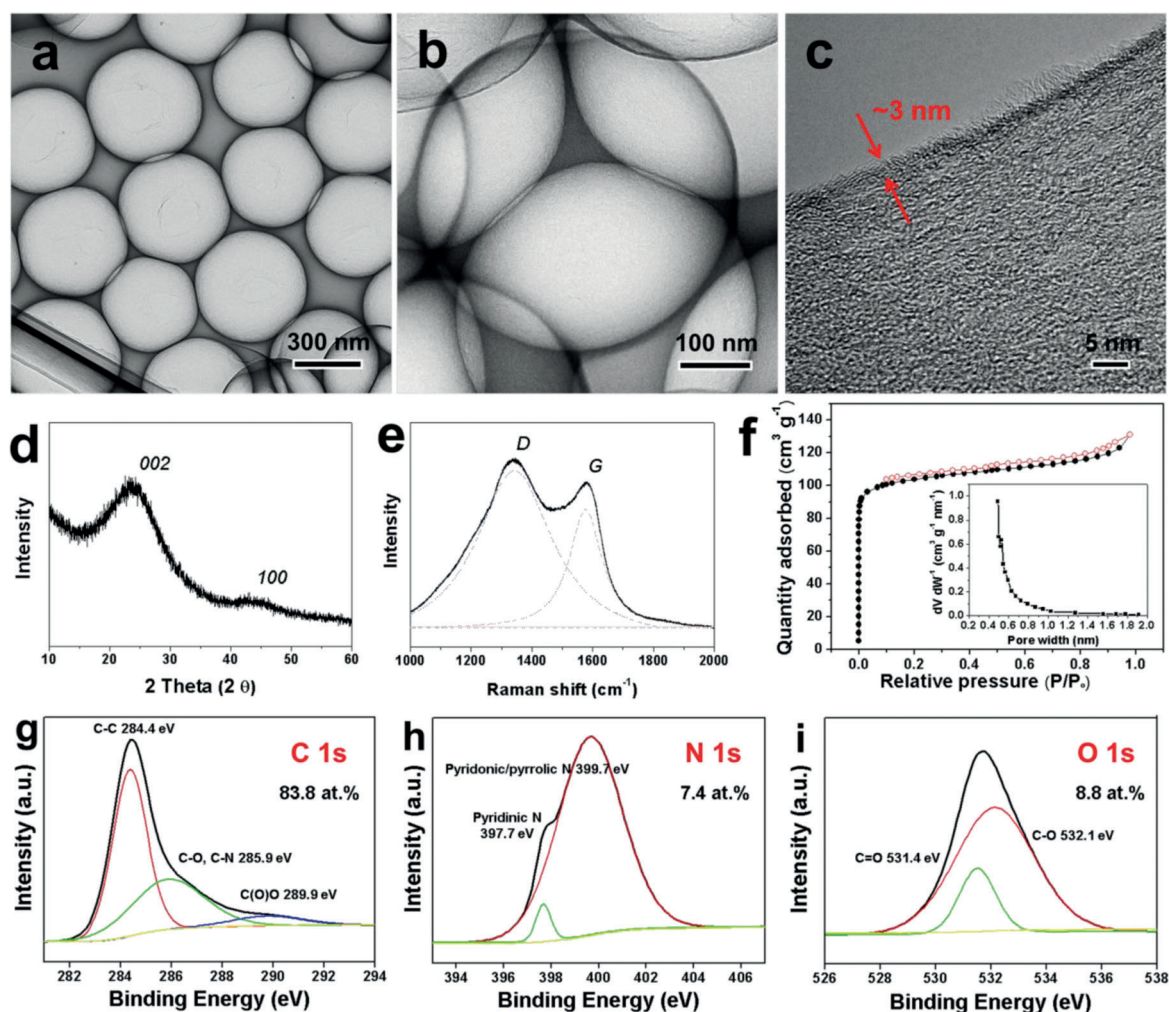
Figure 2. a–c) FE-TEM images showing the morphology of the UTH-CN. d) XRD spectrum and e) Raman spectrum of the UTH-CNs and graphitic crystals. f) Nitrogen adsorption and desorption isotherm curves indicating an IUPAC type I microporous structure and minimal presence of mesopores with a narrow slit-like structure. The width of the micropores are sub-nanometer, as shown in the inset. g) XPS C 1s spectra of the UTH-CNs, revealing the presence of numerous heteroatoms, including nitrogen and oxygen. XPS h) N 1s and i) O 1s spectra, revealing the various chemical configurations in the UTH-CNs.

through small domains are not expected to be favorable for rapid electron transport.

The electrical conductivity of the UTH-CNs was measured using a four-probe method. The bulk electrical conductivity was 2.8 S cm^{-1}, which is large for amorphous carbon, and this is attributed to doping with nitrogen. The X-ray photoelectron spectroscopy (XPS) C 1s spectrum in Figure 2 g reveals several distinct peaks, including peaks corresponding to C—O and C—N bonds centered at 285.9 eV, a C(O)O peak centered at 289.9 eV, and a main C—C peak at 284.4 eV. The nitrogen atoms in the UTH-CNs are mostly pyridonic/pyrrolic with a relatively small number of pyridinic moieties, as indicated by the N 1s peaks centered at 399.7 eV and 397.7 eV, respectively, as shown in Figure 2 h. Nitrogen is present in six-membered and five-membered rings at the edge of the graphene sheet. The XPS analysis shows an atomic concentration of nitrogen of 7.4 at %, and elemental analysis (EA) gives a nitrogen concentration of 9.1 wt %. These results suggest that most of the edges of the graphitic structures are functionalized with nitrogen moieties. In addition, two distinct peaks in the O 1s spectrum shown in

Figure 2 i reveal the presence of oxygen atoms in carbonyl groups (531.4 eV), as well as various other functionalities (532.1 eV). The concentration of oxygen was 8.8 at %, as determined from the XPS data, and was 12.1 wt % as determined from the EA data.

The sodium-ion insertion and extraction behavior in the UTH-CN electrodes was first investigated using a half-cell configuration, with metallic sodium used as a reference electrode and counter electrode. As shown in Figure 3 a, the sodium insertion curve (discharge profile) exhibits a continuous decrease in voltage with no distinct plateaus in the potential range of 0.005–1.5 V versus Na$^+$/Na. The charge profile also exhibits a linear increase in voltage with slight hysteresis. These results suggest that sodium ions are stored in various electrochemically nonequivalent sites in the disordered graphitic carbon structure. The lack of equivalence in the electrochemical potential of sodium may also be attributed to the presence of the heteroatoms, which leads to a loss of orders in the local environments of graphitic structures.[23–25] A reversible discharge capacity of 285 mAh g^{-1} was obtained with a specific current of
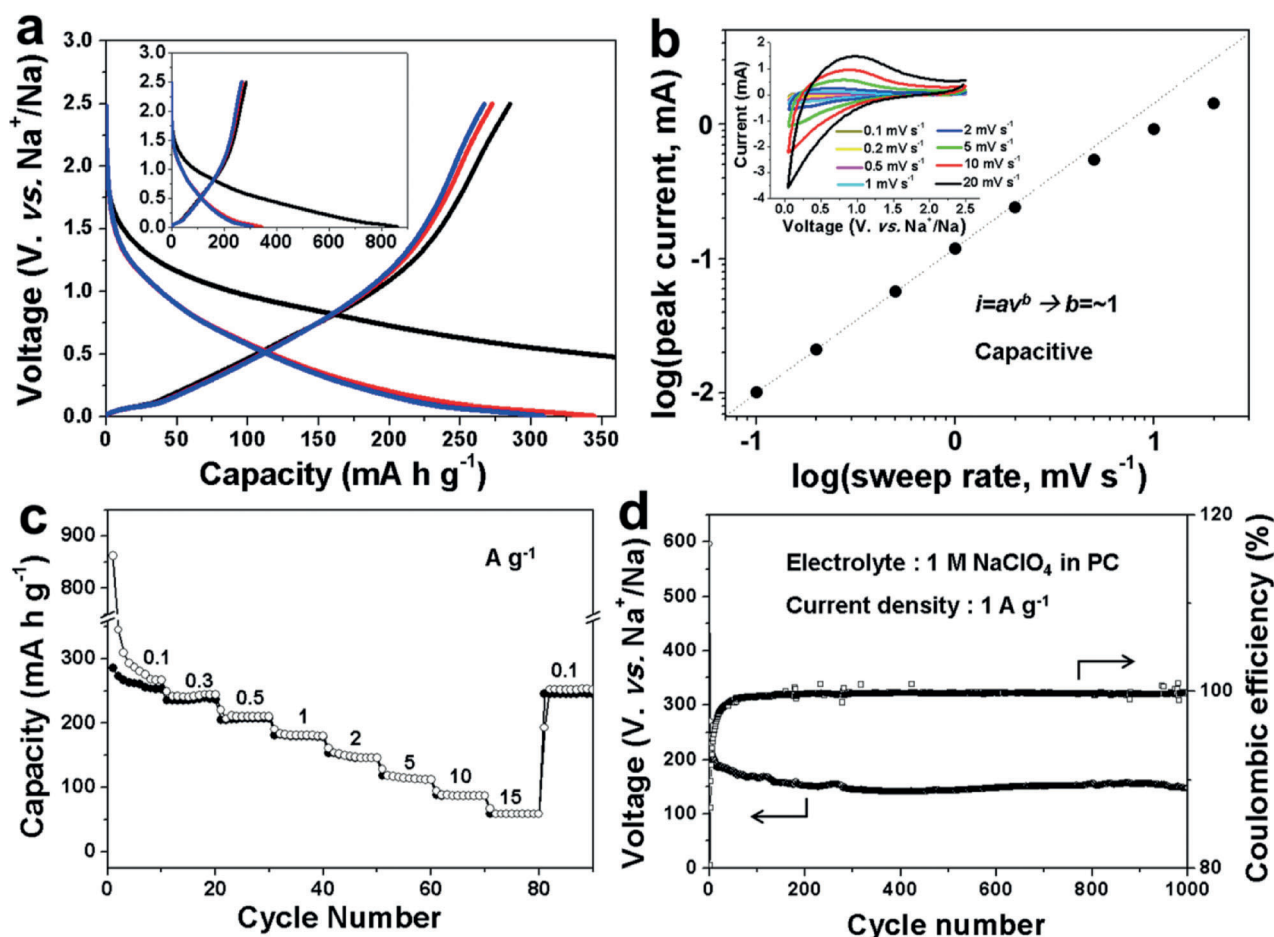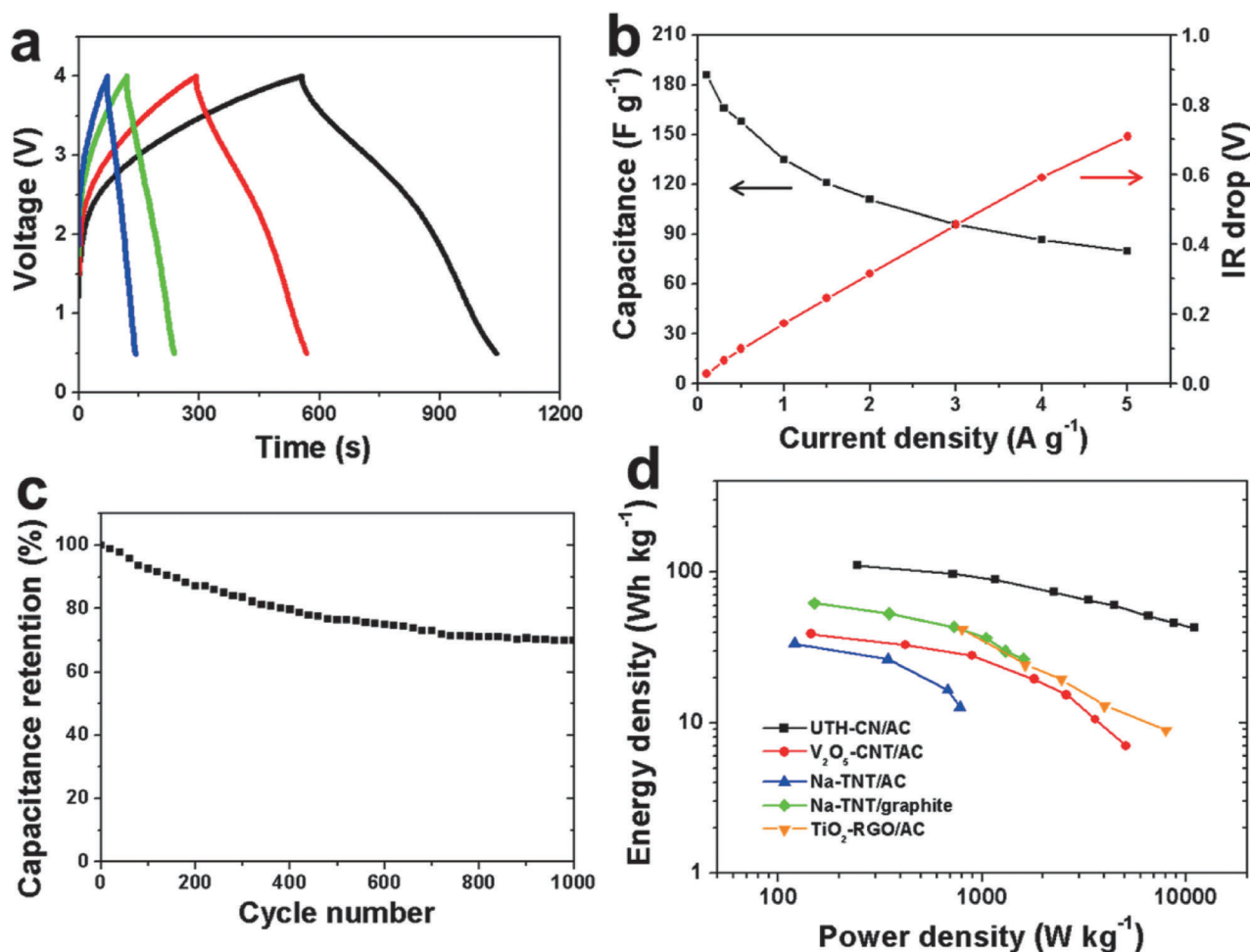
Figure 3. Electrochemical analyses of UTH-CNs in an electrolyte of 1 M NaClO$_4$ dissolved in PC. a) Galvanostatic charge/discharge profiles of the first (black), second (red), and third (blue) cycles. The y-axis shows the potential versus Na/Na$^+$, and the specific current is 100 mA g^{-1}. b) The dependence of the voltammetric current on the sweep rate. The inset shows cyclic voltammograms at various sweep rates in the range 0.1–20 mV s^{-1}. c) Reversibility and rate performance at specific currents the range 0.1–15 A g^{-1}. d) Cyclic performance at 1 A g^{-1} over 1,000 charge/discharge cycles.

100 mA g^{-1}, corresponding to a specific capacitance of 410 F g^{-1}. This is considerably larger than that measured accordingly via surface charge adsorption/desorption (see Figure S3). It follows that sodium storage occurs via pseudocapacitive reactions within a few graphitic layers of the surface. The first irreversible capacity is likely induced from the formation of a solid electrolyte interphase (SEI).

The sodium-ion storage behavior was further investigated by cyclic voltammetry (CV), with sweep rates in the range of 0.1–20 mV s^{-1}, as shown in Figure 3b. Assuming that the current obeys a power-law relationship as a function of the voltage during the sweep, where $i = av^b$, and a and b are constants, the data can be fitted with $b \sim 1$, which indicates that the electrochemical reaction is mostly surface-controlled.[40,41] It also shows that sodium-ion storage in the UTH-CNs is pseudocapacitive in the anodic potential range. We believe that this pseudocapacitive behavior is due to the random distribution of graphitic domains and the short diffusion length through the hollow structure of UTH-CNs, which enables rapid ion transfer, as shown schematically in Figure S4.[22] In addition, the nitrogen functional groups at the edges of graphene sheets may contribute to the pseudocapacitive sodium-ion storage of

UTH-CNs.[23–25] The rate performance of the UTH-CNs for specific currents in the range of 0.1–15 A g^{-1} is shown in Figure 3c. A stable capacity of approximately 75 mAh g^{-1} was obtained with a high current rate of 15 A g^{-1}. In addition, the initial capacity was retained when the current was reduced to 0.1 A g^{-1}. The cycling performance at 1 A g^{-1} was remarkably stable, with a Coulombic efficiency of close to 100% after 1000 cycles, as shown in Figure 3d. A specific capacity of 150 mAh g^{-1} was obtained at 1 A g^{-1} after 1000 cycles.

Full cell tests were carried out using the UTH-CNs as the anode and amorphous carbons (ACs) as the cathode. The sodium-ion storage behavior of the AC was initially tested at a specific current of 1 A g^{-1}, and at potentials ranging from 2 V to 4.5 V. The AC cathode exhibited a specific capacity of 96 mAh g^{-1} with stable cyclic performance (Figure S5). Following pre-cycles of the anode and cathode at potentials in the range 0.005–2 V and 2–4.5 V, respectively, in half-cells, full cells were assembled (Figure S6). The galvanostatic charge/discharge profiles demonstrated reversible sodium-ion storage at various currents, as shown in Figure 4a. The specific capacitance at 100 mA g^{-1} was 186 F g^{-1}, and a specific capacitance of 80 F g^{-1} was maintained at 5 A g^{-1}, as shown in Figure 4b.

Figure 4. Electrochemical analyses of the UTH-CNs/ACs sodium-ion pseudocapacitors in the range of 0.5–4.0 V. a) Galvanostatic charge/discharge profiles at 0.3 A g^{-1} (black), 0.5 A g^{-1} (red), 1 A g^{-1} (green) and 1.5 (blue) A g^{-1}. b) Rate performance and IR drop as a function of the specific current. c) The cycle performance over 1000 charge/discharge cycle with a specific current of 300 mA g^{-1}. d) Ragone plot of various sodium-ion pseudocapacitors, including the UTH-CN/AC described here (black squares), as well as devices based on V$_2$O$_5$-CNT/AC (red circles),[40] Na-TNT/AC (blue triangles),[43] Na-TNT/graphite (green diamonds)[44] and TiO$_2$-RGO/AC (orange inverted triangles).[11]

The IR drops calculated from galvanostatic discharge curves exhibited linear behavior as a function of the current. A potential drop of 0.7 V was measured at 5 A g^{-1}, which is comparable to that of carbon-based symmetric supercapacitors.[42] After 1000 charge/discharge cycles at a constant specific current of 300 mA g^{-1}, approximately 70 % of the initial capacitance was retained in the full cell, as shown in Figure 4c. The gravimetric energy of the asymmetric sodium-ion pseudocapacitor using UTH-CN/AC was estimated as 110 W h kg^{-1} at a gravimetric power of 245 W kg^{-1}, as shown in Figure 4d. With a high power density of 10 kW kg^{-1}, an energy density of 43 W h kg^{-1} was achieved. These energy and power densities are considerably higher than have been previously reported.[40, 43, 44] Furthermore, these performance metrics surpass those values of a lithium-ion based hybrid supercapacitor.[11]

3. Conclusions

We have described H-CNs with extremely thin walls (~3 nm thick) obtained from the biologically occurring polymer RSF

using a template method and heat treatment. The UTH-CNs composed of small graphitic crystals with $L_c \sim 1$ nm and $L_a \sim$ 3.5 nm exhibited a microporous structure and a large specific surface area of 400 m^2 g^{-1}. This highly porous structure showed very promising sodium-ion storage behavior as a pseudocapacitive electrode in asymmetric sodium-ion pseudocapacitors. The asymmetric system paired with a conventional AC could deliver an unprecedentedly high energy density of 110 W h kg^{-1} with a power density of 245 W kg^{-1}. Stable cycle performance was demonstrated, with 70 % of the initial capacitance following 1000 cycles at a specific current of 300 mA g^{-1}.

Experimental Section

The RSF solution was prepared based on the method reported in Ref. [5]. Cocoons were boiled for 30 min in an aqueous solution of 0.02 M Na$_2$CO$_3$ (OCI company Ltd., 99 %), and rinsed thoroughly with water to extract the glue-like sericin proteins. The extracted silk was then dissolved in an aqueous 9.3 M LiBr solution (Sigma–Aldrich, 99 %) at room temperature to yield a 20 wt % solution.

This solution was dialyzed in water using Slide-a-Lyzer dialysis cassettes (Pierce, MWCO 3500) for 36 h. A dilute aqueous solution of NaOH was then added to 20 g 0.1 wt% solution of RSF until a pH of 12 was achieved. A 20 g aqueous dispersion containing 200 mg silica nanospheres (SNSs) was prepared separately via ultrasonication. Then, the SNS dispersion was poured into the RSF solution with vigorous stirring for 30 min, and the mixture was cooled to −196 °C. The frozen RSF/SNS mixture was freeze-dried using a lyophilizer at −50 °C and 0.045 mbar for 72 h. The RSF-coated SNS cryogels were dispersed in water and sonicated for 5 min, after which the dispersion was rapidly poured into a methanol bath. After 6 h, the mixture was vacuum-filtered and dried in a vacuum oven at 30 °C for 24 h. The isolated particulates were then heated from room temperature to 800 °C at a rate of 10 °C min^{-1} under an argon environment, with an argon flow of 200 mL min^{-1}. Once the sample reached 800 °C, this temperature was maintained for 2 h. The isolated particulates were then treated with 30 wt% hydrofluoric acid (HF) solution, and washed with water and ethanol. The yield of UTH-CN product was approximately 5–8 wt% (vs initial RSF contents). The UTH-CNs were stored in a vacuum oven at 30 °C.

The morphology of the UTH-CN was observed using field-emission transmission electron microscopy (FE-TEM) (JEM2100F, JEOL, Japan). X-ray diffraction (XRD) (Rigaku DMAX 2500) analysis was performed using Cu-Kα radiation (with a wavelength $\lambda = 0.154$ nm) at 40 kV and 100 mA. Raman spectroscopy was carried out using a continuous-wave linearly polarized laser with a wavelength of 514 nm, a 50 μm diameter pinhole, and a 600 groove/mm grating. The porosity was analyzed using nitrogen adsorption and desorption isotherms obtained from a surface area and a porosimetry analyzer (ASAP 2020, Micromeritics, USA) at −196 °C. Elemental analysis (EA) was carried out using an EA1112 (CE Instrument, Italy). XPS (PHI 5700 ESCA) was performed using monochromated Al-Kα radiation ($h\nu = 1486.6$ eV). Infrared (IR) spectroscopy was carried out using a VERTEX 80v (Bruker Optics, Germany). The electrical properties were characterized using an electrical conductivity meter (Loresta GP, Mitsubishi Chemical, Japan) using compressed pellets that were 13 mm in diameter. The pellets were prepared by pressing the UTH-CN samples in a stainless steel mold at a pressure of 10 Mpa.

The electrochemical properties of UTH-CNs, commercially available porous carbons (ACs) (MSP-20), and the UTH-CN/AC hybrid capacitors were characterized using a Wonatec automatic battery cycler and CR2032-type coin cells. For the half-cell tests, the coin cells were assembled with either UTH-CN or AC as the working electrode, and metallic sodium foil as both the reference and counter electrodes in a glove box filled with argon. NaClO$_4$ (1 M; Aldrich, purity: 99.99%) was dissolved in a solution of propylene carbonate, and was used as the electrolyte. The working electrodes were prepared by mixing the active material (80 wt%) with conductive carbon (10 wt%) and polyvinylidene fluoride (10 wt%) in N-methyl-2-pyrrolidone. The resulting slurries were uniformly applied to the Al foil. The electrodes were dried at 120 °C for 2 h and roll-pressed. The asymmetric sodium-ion pseudocapacitors based on UTH-CN/AC were assembled using pre-cycled UTH-CNs as the anode, and ACs as the cathode. The voltage was controlled to 2 V versus Na$^+$/Na. The pseudocapacitors were galvanostatically cycled between 0.5 V and 4.0 V at various currents. The mass loadings of UTH-CNs and ACs were 2 mg and 4 mg, respectively, in full cells. The Ragone plot was calculated based on the whole mass of both electrodes.

[1] M. Armand, J.-M. Tarascon, *Nature* **2008**, *451*, 652–657.
[2] J. Tollefson, *Nature* **2008**, *456*, 436–440.
[3] J.-M. Tarascon, *Nat. Chem.* **2010**, *2*, 510.
[4] S. W. Lee, B. M. Gallant, H. R. Byon, P. T. Hammond, Y. Shao-Horn, *Energy Environ. Sci.* **2011**, *4*, 1972–1985.
[5] Y. S. Yun, S. Y. Cho, J. Shim, B. H. Kim, S.-J. Chang, S. J. Baek, Y. S. Huh, Y. Tak, Y. W. Park, S. Park, H.-J. Jin, *Adv. Mater.* **2013**, *25*, 1993–1998.
[6] V. Etacheri, R. Marom, R. Elazari, G. Salitra, D. Aurbach, *Energy Environ. Sci.* **2011**, *4*, 3243–3262.
[7] J. Hassoun, K.-S. Lee, Y.-K. Sun, B. Scrosati, *J. Am. Chem. Soc.* **2011**, *133*, 3139–3143.
[8] R. Mukherjee, R. Krishnan, T.-M. Lu, N. Koratkar, *Nano Energy* **2012**, *1*, 518–533.
[9] Y. Zhu, S. Murali, M. D. Stoller, K. J. Ganesh, W. Cai, P. J. Ferreira, A. Pirkle, R. M. Wallace, K. A. Cychosz, M. Thommes, D. Su, E. A. Stach, R. S. Ruoff, *Science* **2013**, *332*, 1537–1541.
[10] Y. S. Yun, M. E. Lee, M. J. Joo, H.-J. Jin, *J. Power Sources* **2013**, *246*, 540–547.
[11] H. Kim, M.-Y. Cho, M.-H. Kim, K.-Y. Park, H. Gwon, Y. Lee, K. C. Roh, K. Kang, *Adv. Energy Mater.* **2013**, *3*, 1500–1506.
[12] J. Ni, Y. Huang, L. Gao, *J. Power Sources* **2013**, *223*, 306–311.
[13] F. Zhang, T. Zhang, X. Yang, L. Zhang, K. Leng, Y. Huang, Y. Chen, *Energy Environ. Sci.* **2013**, *6*, 1623–1632.
[14] H. Kim, K.-Y. Park, M.-Y. Cho, M.-H. Kim, J. Hong, S.-K. Jung, K. C. Roh, K. Kang, *ChemElectroChem.* **2014**, *1*, 125–130.
[15] L. Qie, W.-M. Chen, Z.-H. Wang, Q.-G. Shao, X. Li, L.-X. Yuan, X.-L. Hu, W.-X. Zhang, Y.-H. Huang, *Adv. Mater.* **2012**, *24*, 2047–2050.
[16] B. Z. Jang, C. Liu, D. Neff, Z. Yu, M. C. Wang, W. Xiong, A. Zhamu, *Nano Lett.* **2011**, *11*, 3785–3791.
[17] Z. Fan, Y. Liu, J. Yan, G. Ning, Q. Wang, T. Wei, L. Zhi, F. Wei, *Adv. Energy Mater.* **2012**, *2*, 419–424.
[18] H. Zhang, G. Cao, Y. Yang, *Energy Environ. Sci.* **2009**, *2*, 932–943.
[19] S. Yang, X. Feng, L. Zhi, Q. Cao, J. Maier, K. Müllen, *Adv. Mater.* **2010**, *22*, 838–842.
[20] F.-D. Han, Y.-J. Bai, R. Liu, B. Yao, Y.-X. Qi, N. Lun, J.-X. Zhang, *Adv. Energy Mater.* **2011**, *1*, 798–801.
[21] K. Wang, Z. Li, Y. Wang, H. Liu, J. Chen, J. Holmes, H. Zhou, *J. Mater. Chem.* **2010**, *20*, 9748–9753.
[22] P. Simon, Y. Gogotsi, B. Dunn, *Science* **2014**, *343*, 1210–1211.
[23] K. Tang, L. Fu, R. J. White, L. Yu, M.-M. Titirici, M. Antonietti, J. Maier, *Adv. Energy Mater.* **2012**, *2*, 873–877.
[24] Z. Wang, L. Qie, L. Yuan, W. Zhang, X. Hu, Y. Huang, *Carbon* **2013**, *55*, 328–334.
[25] H.-G. Wang, Z. Wu, F.-L. Meng, D.-L. Ma, X.-L. Huang, L.-M. Wang, X.-B. Zhang, *ChemSusChem* **2013**, *6*, 56–60.
[26] D. A. Stevens, J. R. Dahn, *J. Electrochem. Soc.* **2001**, *148*, A803–A811.
[27] S. H. Lim, H. I. Elim, X. Y. Gao, A. T. S. Wee, W. Ji, J. Y. Lee, J. Lin, *Phys. Rev. B* **2006**, *73*, 045402.
[28] R. Czerw, M. Terrones, J.-C. Charlier, X. Blase, B. Foley, R. Kamalakaran, N. Grobert, H. Terrones, D. Tekleab, P. M. Ajayan, W. Blau, M. Rühle, D. L. Carroll, *Nano Lett.* **2001**, *1*, 457–460.

[29] Y. S. Yun, C. Im, H. H. Park, I. Hwang, Y. Tak, H.-J. Jin, *J. Power Sources* **2013**, *234*, 285 – 291.

[30] H.-J. Jin, D. L. Kaplan, *Nature* **2003**, *424*, 1057 – 1061.

[31] H.-J. Jin, J. Chen, V. Karageorgiou, G. H. Altman, D. L. Kaplan, *Biomaterials* **2004**, *25*, 1039 – 1047.

[32] X. Wang, T. Yucel, Q. Lu, X. Hu, D. L. Kaplan, *Biomaterials* **2010**, *31*, 1025 – 1035.

[33] S.-M. Kwon, H.-S. Kim, H.-J. Jin, *Polymer* **2009**, *50*, 2786 – 2792.

[34] S.-K. Chae, E. Kang, A. Khademhosseini, S.-H. Lee, *Adv. Mater.* **2013**, *25*, 3071 – 3078.

[35] M. A. Brenckle, H. Tao, S. Kim, M. Paquette, D. L. Kaplan, F. G. Omenetto, *Adv. Mater.* **2013**, *25*, 2409 – 2414.

[36] H.-S. Kim, S. H. Yoon, S.-M. Kwon, H.-J. Jin, *Biomacromolecules* **2009**, *10*, 82 – 86.

[37] A. Rimola, D. Costa, M. Sodupe, J.-F. Lambert, P. Ugliengo, *Chem. Rev.* **2013**, *113*, 4216 – 4313.

[38] M. Lundqvist, P. Nygren, B.-H. Jonsson, K. Broo, *Angew. Chem. Int. Ed.* **2006**, *45*, 8169 – 8173; *Angew. Chem.* **2006**, *118*, 8349 – 8353.

[39] E. J. Bottani, J. M. D. Tascon, *Adsorption by Carbon*, Elsevier, Jordan Hill, Oxford, **2008**, pp. 15 – 49.

[40] Z. Chen, V. Augustyn, X. Jia, Q. Xiao, B. Dunn, Y. Lu, *ACS Nano* **2012**, *6*, 4319 – 4327.

[41] V. Augustyn, J. Come, M. A. Lowe, J. W. Kim, P.-L. Taberna, S. H. Tolbert, H. D. Abruña, P. Simon, B. Dunn, *Nat. Mater.* **2013**, *12*, 518 – 522.

[42] A. Izadi-Najafabadi, S. Yasuda, K. Kobashi, T. Yamada, D. N. Futaba, H. Hatori, M. Yumura, S. Iijima, K. Hata, *Adv. Mater.* **2010**, *22*, E235 – E241.

[43] J. Yin, L. Qi, H. Wang, *ACS Appl. Mater. Interfaces* **2012**, *4*, 2762 – 2768.

[44] L. Zhao, L. Qi, H. Wang, *J. Power Sources* **2013**, *242*, 597 – 603.